Durable, pure-water-fed, anion-exchange-membrane electrolyzers through interphase engineering

Shujin Hou[1,2], Archana Sekar[3], Yang Zhao[1,2], Minkyoung Kwak[1,4], Juhyun Oh[5], Kelvin Kam-Yun Li[1,6,7], Peiyao Wu[1], Ryan T. Hannagan[8,9], Valeria Cartagena[8,9], Anthony C. Ekennia[1,4], Hui Duan[10], Michael J. Zachman[5], Joelle Frechette[1,2], Gregory M. Su[6,7], Balsu Lakshmanan[3], Yushan Yan[10], Thomas F. Jaramillo[8,9], and Shannon W. Boettcher[1,2,4*]

[1]Department of Chemical & Biomolecular Engineering and Department of Chemistry, University of California, Berkeley, CA, USA.

[2]Energy Storage and Distributed Resources Division, Lawrence Berkeley National Laboratory, Berkeley, CA, USA.

[3]Versogen, Newark, DE, USA.

[4]Oregon Center for Electrochemistry, Department of Chemistry and Biochemistry, University of Oregon, Eugene, OR, USA.

[5]Center for Nanophase Materials Sciences, Oak Ridge National Laboratory, Oak Ridge, TN, USA.

[6]Materials Sciences Division, Lawrence Berkeley National Laboratory, Berkeley, CA, USA.

[7]Advanced Light Source, Lawrence Berkeley National Laboratory, Berkeley, CA, USA.

[8]Department of Chemical Engineering, Stanford University, Stanford, CA, USA.

[9]SUNCAT Center for Interface Science and Catalysis, SLAC National Accelerator Laboratory, Menlo Park, CA, USA.

[10]Department of Chemical and Biomolecular Engineering, Center for Clean Hydrogen, University of Delaware, Newark, DE, USA.

*Corresponding author. Email: boettcher@berkeley.edu

Abstract: Anion-exchange-membrane water electrolyzers (AEMWEs) promise scalable low-cost hydrogen production but are limited by the electrochemical instability of their anode ionomers. We report interphase engineering using inorganic-containing molecular additives that co-assemble with ionomer, enabling pure-water-fed AEMWEs to operate with a degradation rate < 0.5 $mV \cdot h^{-1}$ at an industry-relevant 2.0 $A \cdot cm^{-2}$ and 70 °C – a > 20-fold durability improvement. Analysis of different additives and ionomers shows that the stabilization mechanism involves crosslinks between metal oxo/hydroxo oligomers and ionomers. Under operation, the inorganic additive enriches, forming an interphase near the water-oxidation catalyst that passivates the anode ionomer against continuous degradation while maintaining mechanical integrity and hydroxide conductivity. This additive-based interphase-engineering strategy provides a path to durable AEMWEs that operate without supporting electrolytes and is adaptable across diverse catalysts and ionomers for electrochemical technologies.

Main Text: Anion-exchange-membrane (AEM) water electrolyzers (WEs) offer electrochemical output-gas compression (*1, 2*), load-following/start-stop operation (*3, 4*), pure-water feed (*5*), and the possibility of using hydrocarbon ionomer membranes (*1, 6*), non-precious-metal catalysts (*7, 8*), and low-cost stack components (*1, 9*). AEMWE is thus a possible disruptive technology to enable H_2 production to outcompete fossil-fuel-derived H_2 on cost (*10, 11*). While the performance of research-scale and commercial systems has improved, durability remains a major issue, especially when operating without soluble supporting electrolytes as is needed to simplify the balance of plant (*12*) and eliminate shunt currents and reverse-polarization (*13, 14*).

The ionomers used in AEMWEs contain fixed-charge groups, typically quaternary-ammonium cations with effective concentrations >1 M. The mobile hydroxide counterions (OH^-) carry the ionic current through the porous electrode and membrane phases (*15, 16*). Historically, these ionomers have been susceptible to degradation by Hofmann elimination and nucleophilic attack of OH^- on the cationic group or backbone (*10, 17, 18*) due to the more-aggressive alkaline environment compared to acidic conditions. Modern ionomer chemical designs mitigate the attack of OH^- using steric and electronic effects (*7, 19-25*). Yet, when these ionomers are used in AEMWEs as the membrane, and within the ionomer/catalyst-containing porous electrodes, the durability is poor with degradation rates typically >>1 mV/h even at a current density of ≤ 1 A cm^{-2} (*3, 5, 13, 26-30*). Such performance is not competitive with proton-exchange-membrane electrolyzers (PEMWEs) that operate at 2–4 A cm^{-2} at < 2 V and with < 10 μV/h degradation rates (*31, 32*).

The primary degradation mode in pure-water-fed AEMWE is the oxidation of the ionomer within the anode catalyst layer under the locally alkaline conditions where even the most-robust perfluorinated ionomers degrade (*13, 33*). Ionomer oxidation leads to increased ohmic resistance through the loss of OH^- transport pathways (*34, 35*), dissolution of transition-metal catalysts driven by decreased local pH as the basic quaternary ammonium groups are degraded (*36-38*), and mechanical disintegration and catalyst detachment from compromised binding properties of the ionomer (*36*). Recent prototypes for commercial AEMWE systems circumvent this issue by flooding the anode with a soluble KOH electrolyte that carries the ionic current (*1, 5*), in addition to the ionomer binder, resulting in a hybrid device that mixes elements of traditional liquid-alkaline and membrane electrolyzers. Even in supporting electrolyte, however, the oxidation rate is non-zero. The supporting electrolyte masks this degradation, particularly over shorter tests, by maintaining conformal OH^- transport to the catalyst (*37, 39, 40*). The hybrid approach also negates advantages of a pure-water feed, including the simplified balance of plant, lower-cost materials, and lack of reverse polarization (*13*). The development of new anode and ionomer interfacial strategies to suppress oxidation of ionomers is thus central to making AEMWEs a disruptive technology.

Li-ion batteries also feature reactive electrodes that degrade organic electrolyte and salts (*41-43*). This problem has been solved in commercial Li-ion batteries through a combination of electrolyte additives that decompose on the reactive electrodes to form organic-inorganic solid-electrolyte-interphase (SEI) layers that passivate the electrode against continuous electrolyte decomposition (*43, 44*). The SEI is conductive to Li^+ but blocks electronic current that would otherwise result in catastrophic electrolyte decomposition (*45*). While the interphase designs will differ, conceptually similar SEI-engineering approaches may be much more broadly applicable in stabilizing electrodes in electrochemical technology.

Here we show that metal-alkoxide inorganic additives generate oxo/hydroxo oligomers that can be tuned to co-assemble with ionomers during electrode fabrication and form durability enhancing interphases. The most-effective Zr-based additives create inorganic crosslinks in the ionomer phase that improve stability of the electrode more than ten-fold. These layers limit interfacial degradation through formation of Zr-oxo/hydroxo-enriched interphases that appear resistant to oxidation and electron transport, but have high OH^- conductivity and no detrimental effect on the catalyst's water-oxidation kinetics. With this interphase-engineering strategy, we show a pure-water-fed AEMWE operating for >400 h at 2.0 A cm^{-2} at 70 °C degrading at < 0.5 mV h^{-1}. The approach is versatile and compatible with many catalysts, metal-alkoxide or other inorganic additives, and ionomers. The work provides a new science-informed pathway to practical AEMWEs that may, with further development, outcompete PEMWEs on performance and traditional liquid-alkaline electrolyzers on cost. This additive and interphase-engineering approach is broadly relevant to enhancing the durability of other ionomer-based electrochemical devices that operate in harsh environments.

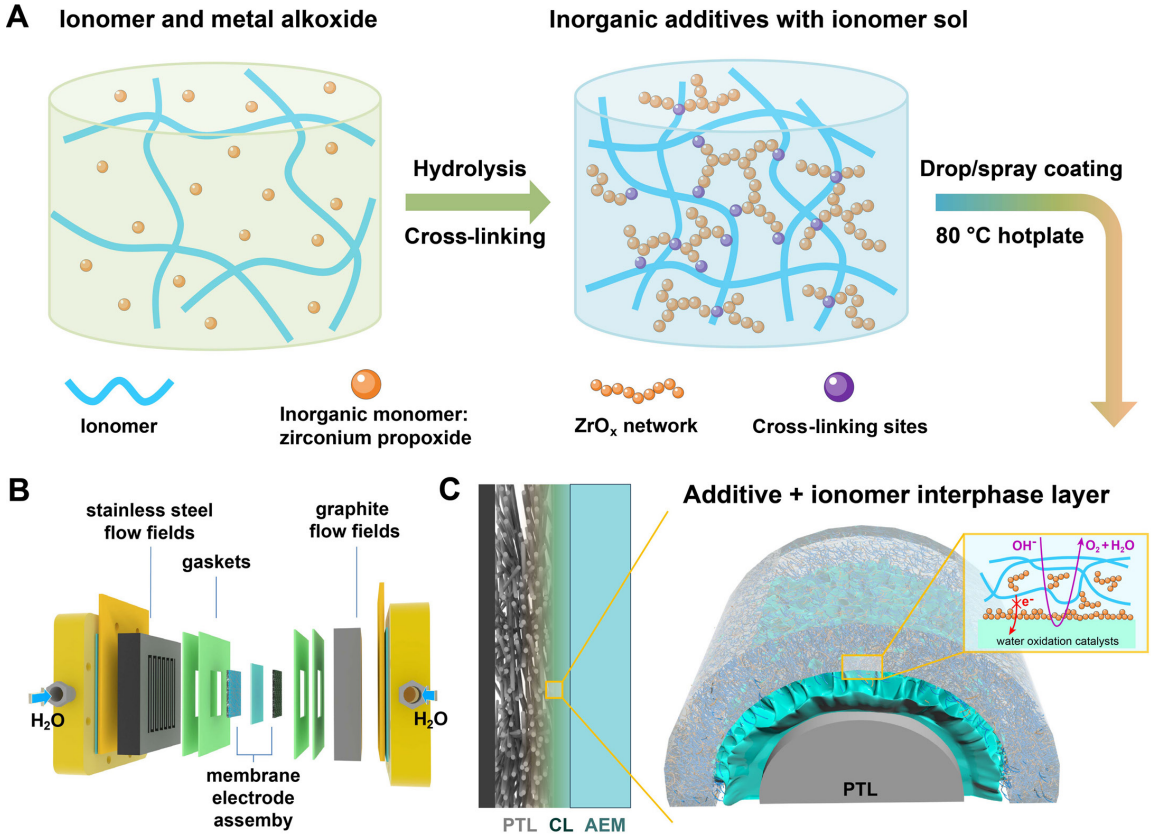

Fig. 1. Engineering a solid-electrolyte interphase in AEMWE. (**A**) Preparation of organic/inorganic gel by cross-linking ionomer and zirconium oxo/hydroxy oligomers. (**B**) Schematic of pure-water-fed AEMWE single cell. (**C**) Schematic of the hypothesized additive/ionomer interphase structure located between the ionomer and the anode catalyst. The cylindrical shape represents the stainless-steel fiber that comprises the PTL, which is conformally coated by nanosheet shaped catalyst prior to additive + ionomer infilling.

Design of additives/ionomer interphase

The chemistry underlying the preparation of durable anodes is shown in Fig. 1 using zirconium propoxide additive, $Zr(OPr)_4$, as an example, with PiperION® anion-exchange ionomer. When the

transparent, yellowish ionomer dispersion is added to $Zr(OPr)_4$, the mixture turns milky white (Fig. S1) as the metal alkoxides partially hydrolyze, $Zr(OPr)_4 + H_2O \rightarrow Zr(OH)(OPr)_3 + PrOH$ (*46*), and react with the bicarbonate counterions, $Zr(OPr)_4 + HCO_3^- \rightarrow Zr(OPr)_3(CO_3)^- + PrOH$ (*47*). These new species condense to form oligomers, *e.g.*, via $Zr(OPr)_{n-1}(OH) + Zr(OPr)_{n-1}(OH) \rightarrow Zr(OPr)_{n-1}{-}O{-}Zr(OPr)_{n-1} + H_2O$. Simultaneously, the hydrolyzed inorganic species interact with the organic ionomers, forming chemical crosslinks (see below). The resulting inorganic-oligomer/ionomer dispersion is then coated at 80 °C onto the anode catalysts (here typically CoO_x-based) that are grown directly on a Ni or steel porous transport layer (PTL). As alcohol/water evaporates, polycondensation is promoted and a crosslinked inorganic-organic hybrid interphase that has improved oxidative resistance and mechanical adhesion is formed (Fig. 1C).

Performance of AEMWEs without soluble supporting electrolyte

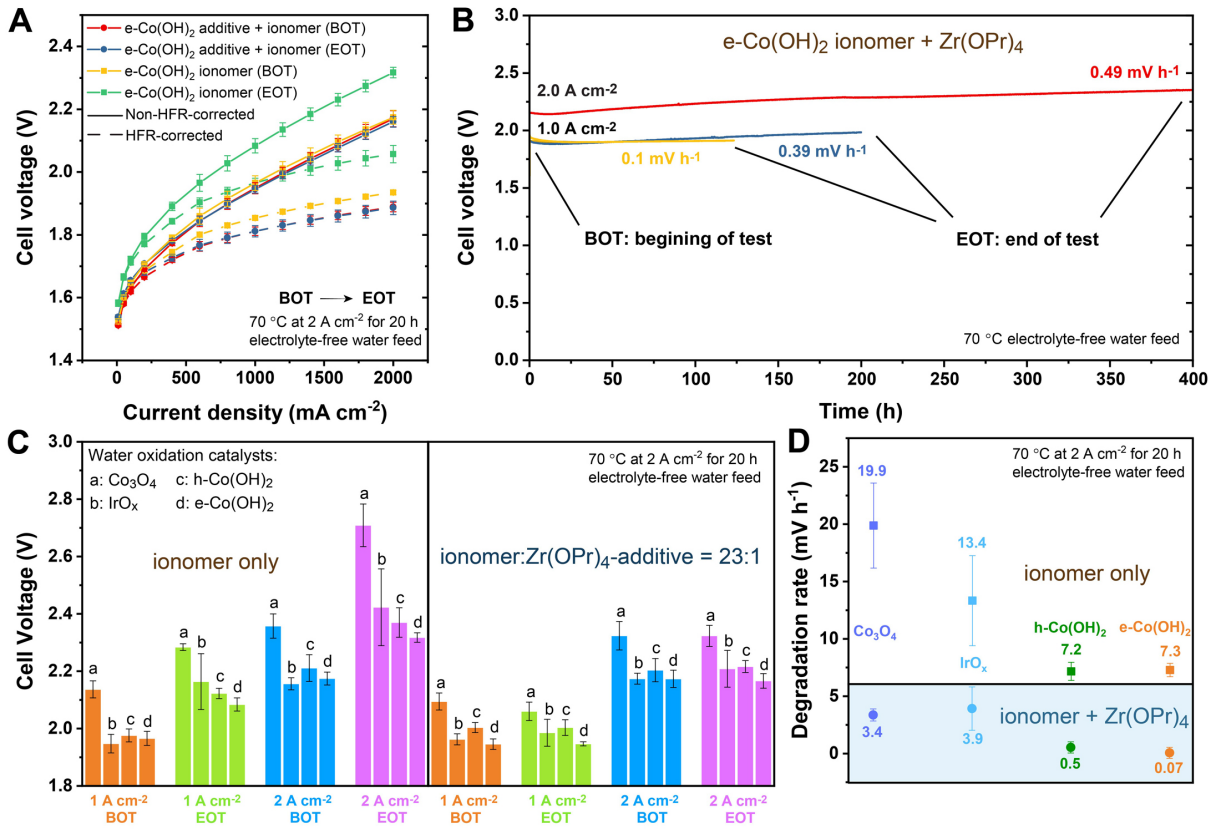

Fig. 2. AEMWE polarization when fed pure water. (**A**) Beginning-of-test (BOT) and end-of-test (EOT) polarization curves of AEMWE cells with electrodeposited cobalt hydroxide (e-$Co(OH)_2$) as the anode catalyst layer interfaced with either ionomer or an ionomer/additive mixture for a 20-h test at 2.0 A cm^{-2} and 70 °C. Pure water (18.2 MΩ·cm) was used as the feed. The dashed lines represent the high-frequency resistance (HFR)-corrected polarization curves before and after the 20-h durability tests. (**B**) Chronopotentiometry stability test using additives/ionomer coated e-$Co(OH)_2$ anodes at 1.0 and 2.0 A cm^{-2}, where the device tests were ended after 123, 200, and 400 h without device failure. (**C**) BOT and EOT cell voltages at 1.0 and 2.0 A cm^{-2} for different anode catalysts. The left panel shows results for ionomer alone and the right panel with additives. This durability test was carried out at 70 °C for 20 h in pure-water feed. Commercial Co_3O_4, IrO_x, hydrothermally synthesized cobalt hydroxide (h-$Co(OH)_2$), and e-$Co(OH)_2$ were loaded onto stainless-steel PTL as the anode catalysts. (**D**) Degradation rates of AEMWEs using above four different anode catalysts over 20 h at a current density of 2.0 A cm^{-2}, each showing dramatic improvements in durability with the additive-derived interphase.

Using electrodeposited cobalt hydroxide (e-$Co(OH)_2$) anode catalyst as an example, we optimized the mass ratio of ionomer and $Zr(OPr)_4$ in the dispersion, showing a two-order-of-magnitude reduction in the degradation rate over the first 20 h compared to ionomer-only coatings (Figs. 2A, 2B, S13A and S15). Beginning-of-test (BOT) voltages decreased with increasing ionomer:$Zr(OPr)_4$ mass ratio, while degradation rates followed a U-shaped trend and minimum of < 0.1 mV h^{-1} over 20 h at 2.0 A cm^{-2} with a ratio of 23:1. For ionomer:$Zr(OPr)_4$ mass ratios < 20, the electrolyzer BOT performance was inferior to that of the ionomer-only system (2.0 A cm^{-2} at 2.17 ± 0.02 V), likely due to insufficient ionomer in the catalyst layer limiting ionic conductivity and causing an increase in the measured high-frequency resistance (Fig. S14). While lower $Zr(OPr)_4$ content improved BOT cell performance, it compromised durability.

Given the three-dimensional structure and distribution of e-$Co(OH)_2$ on/within the PTL (Fig. S16), the method of applying additive/ionomer dispersion has a substantial effect on cell voltage and durability. The lowest degradation rates were achieved by drop casting 1.5 mg cm^{-2} of additives/ionomer on the catalyst-coated PTL, followed by spray coating 1.5 mg cm^{-2} (Fig. S13B). Counterintuitively, three-electrode measurements in 0.10 M KOH showed that coating e-$Co(OH)_2$ with the Zr-additive enhanced the water oxidation activity by ~8% (Fig. S17). The improvement may be due to ZrO_x modifying the catalyst surface chemistry, perhaps increasing hydrophilicity (Fig. S18) under OER conditions (Fig. S18) (*48*). Electrochemical surface-area studies in both electrolyzer and three-electrode systems indicate that incorporating the additive into the ionomer layer has a negligible impact on apparent capacitance but effectively maintains the BOT capacitance after 20-h durability tests (Figs. S22 and S23). On-line inductively coupled plasma mass spectrometry (ICP-MS) showed similar stability of the e-$Co(OH)_2$ during short durability tests with and without additive (Fig. S5), consistent with the hypothesis that the ionomer is the source of instability.

To understand transport through the additives/ionomer interphase layer, we measured the ionic conductivity in the AEMWE (*49, 50*). We sandwiched a layer of ionomer, or ionomer with additives, between two strips of membrane that provided an ionic interconnect to two reference electrodes exterior to the cell. The voltage across the reference electrodes was measured as a function of current through the electrolyzer. The additives/ionomer film had ~12% higher ionic conductivity than ionomer alone under identical conditions (Fig. S19). Similarly, a film containing Zr-additive yielded lateral conductivity of ~190 mS cm^{-1} (80 °C under 100% relative humidity, Fig. S20), higher than that of pristine PAP-TP-85 (~170 mS cm^{-1}) (*19*). We also found the cell-level voltage losses from porous-electrode electronic and ionic transport (*51*) decreased after a short-term durability test when Zr-additive was incorporated in ionomer (Fig. S21), consistent with improved OH^- transport. The ZrO_x is hydrophilic, which appears to drive assembly of water channels and thus improve the internal ion-conducting pathways (see below). Incorporating optimal inorganic additives thus unexpectedly enhances both catalytic activity for water oxidation and ionic transport to those catalytic sites.

During longer-term measurements at 70 °C (Fig. 2B), degradation rates stabilized with an average degradation rate of 0.39 mV h^{-1} at 1.0 A cm^{-2} over 200 h, and 0.49 mV h^{-1} at 2.0 A cm^{-2} over 400 h, with no abrupt cell failure detected. The average degradation rates were 0.31 and 0.80 mV h^{-1} at 1.0 and 2.0 A cm^{-2}, respectively, over the first 120 h. The optimized dispersion with ionomer:$Zr(OPr)_4$ mass ratio of 23 was used with other catalysts including commercial Co_3O_4 and IrO_x powders, hydrothermally synthesized cobalt hydroxide (h-$Co(OH)_2$). For the powder samples, the catalyst layer was fabricated by spray-coating inks containing nanopowder catalyst and

ionomer, followed by spray-coating 2.0 mg cm^{-2} of additives/ionomer as a topcoat. All catalysts with additives/ionomer exhibited BOT cell voltages comparable to ionomer-only counterparts and EOT cell voltages significantly lower (Figs. 2C and S15) with degradation rates reduced by at least 5-fold using the Zr-additive (Fig. 2D).

Microscopic electrocatalyst/interphase/ionomer structure

We studied the structure of the electrode to understand the processes underlying enhanced stability. In the ionomer-only system, electron microscopy and spectroscopy (Figs. S28 to S31) showed the continuous loss of ionomer on the catalyst surface, consistent with measured increases of cell voltage, and ohmic and charge-transfer impedances (Figs. S32 and S33). Ionomer oxidation and dissolution weaken mechanical adhesion and facilitate particle detachment. For cells with optimal $Zr(OPr)_4$, the additives/ionomer interphase layer remained adhered to the electrocatalyst surface even after 20 h at 2.0 A cm^{-2} (Figs. S34 and S35).

Low-dose cryogenic transmission-electron-microscopy (cryo-TEM) was used to study the system. Model electrodes were prepared by depositing e-$Co(OH)_2$ onto Au-mesh TEM grids, subsequently coated with ionomer with, and without, $Zr(OPr)_4$ additive, and operated in the AEMWE cell at 2.0 A cm^{-2} (Fig. S36). The sample with additive displayed distinct, nanometer-scale, dark features within the ionomer and near the e-$Co(OH)_2$ catalyst surface, attributed to amorphous ZrO_x-rich regions (Fig. 3B). The sample without additive showed few high-contrast features (Fig. 3A). Electron energy-loss spectroscopy (EELS) of the e-$Co(OH)_2$-additive/ionomer sample (Fig. S40) showed the Zr L-edge, which was not present in the control sample. Spectral features at the N K-edge associated with quaternary ammonium groups changed little for the e-$Co(OH)_2$-additives/ionomer sample after the 20 h, compared to the e-$Co(OH)_2$-ionomer sample (Fig. S6), consistent with the ZrO_x protecting these groups from oxidative damage (Fig. S8). Time-of-flight secondary-ion-mass spectrometry depth profiles showed a uniform distribution of ZrO_x and ionomer in films coated on a flat Ir/Si control wafer (Fig. S41).

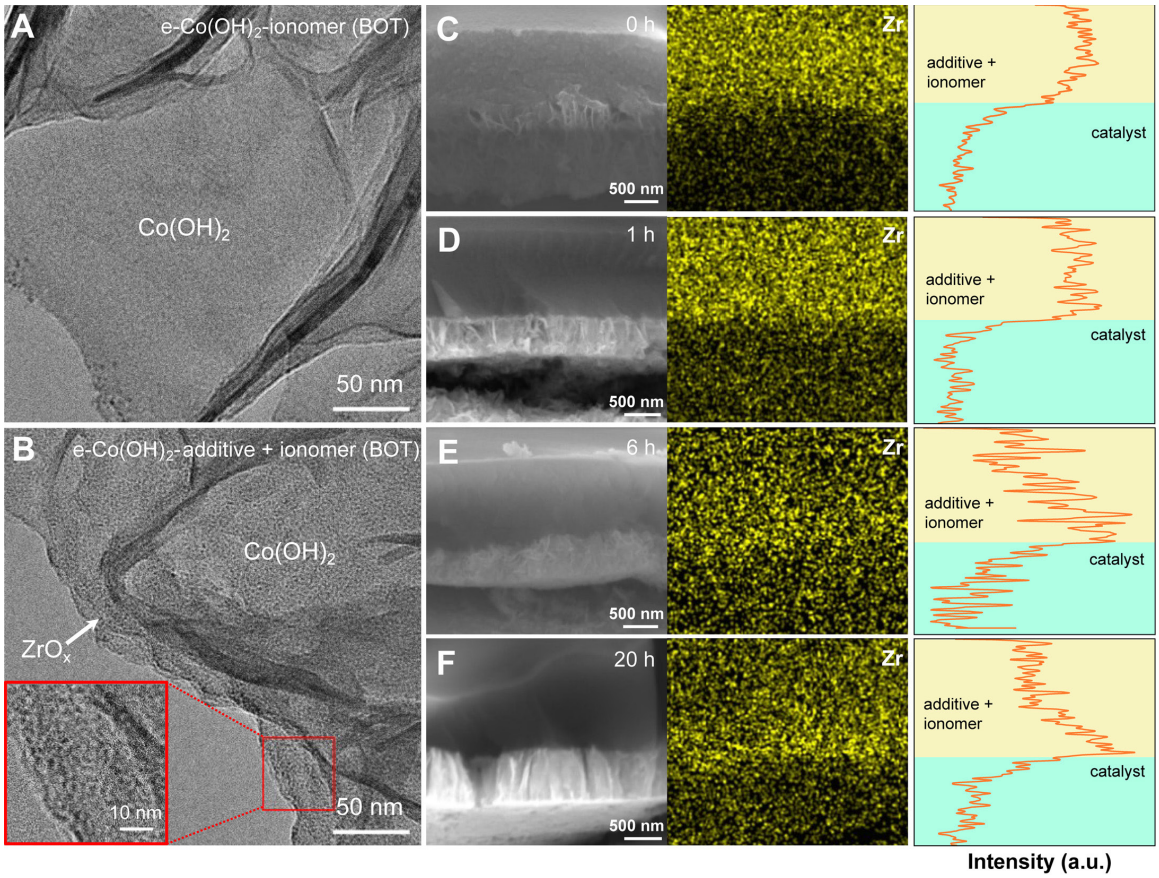

Figure 3. Microscopic evidence of the protective interphase layer. Low-dose cryo-TEM of **(A)** e-$Co(OH)_2$-ionomer and **(B)** e-$Co(OH)_2$-additives/ionomer interphase before electrochemical testing. The inset in **(B)** is a magnified view of the outlined red area, highlighting well-dispersed nanometer-scale dark features consistent with ZrO_x dispersed in the ionomer. These samples were prepared by depositing e-$Co(OH)_2$ onto gold TEM grids, followed by coating of ionomers or additives/ionomer. (**C**–**F**) Cross-sectional SEM images and EDX maps of Zr with corresponding integrated intensity along the direction orthogonal to the catalyst/ionomer interface for **(C)** e-$Co(OH)_2$-additives/ionomer on PTLs and samples after testing at 2.0 A cm^{-2} for **(D)** 1 h, **(E)** 6 h, and **(F)** 20 h.

Cross-sectional maps (Figs. 3C–3F and S42–45) showed Zr uniformly distributed in the pristine samples. After 1 h of operation at 2.0 A cm^{-2}, increased Zr was found in the regions next to the electrocatalyst, consistent with oxidative instability of the ionomer near the catalyst leading to its degradation and dissolution. The remaining ZrO_x-rich interphase is hypothesized to be a porous, hydrated, hydroxide-permeable solid that maintains mechanical stability and adhesion, while electrically insulating against catastrophic oxidative ionomer damage. The accumulation of ZrO_x in the interphase appears critical in preventing runaway interfacial oxidative degradation of the ionomer and associated increased resistance and pH decrease at the catalyst. Control experiments where 0.7 mg cm^{-2} of ionomer was coated on the catalyst surface followed by a top layer of 2 mg cm^{-2} of the optimal ionomer/$Zr(OPr)_4$ dispersion yielded similar initial polarization curves, but fast degradation of ~18 $mV \cdot h^{-1}$ (Fig. S46) like ionomer-only systems (Fig. S32). When ionomer is applied as a topcoat over Zr:ionomer that is in contact with the catalyst, it remains stable over 20 h (Figs. S48 and S49). This is evidence that the primary degradation mode is not chemical OH^- attack, but associated with the oxidizing reaction environment. The oxidative degradation may be either direct, or via a mediated process over a short length scale at the catalysts/ionomer interface.

Although not in direct contact with electrocatalyst, the bulk membrane itself may degrade via nucleophilic-substitution (*e.g.*, attack by OH^-) and Hofmann-elimination reactions, leading to cation and ion-exchange capacity loss (*17, 18*). Oxidative species generated during water oxidation (*e.g.*, hydroxyl radicals, peroxides, and/or soluble high-valent metals) might also transport to the membrane from the catalyst/ionomer region and lead to degradation, for example by backbone chain scission, although evidence for these processes in aryl-ether-free AEMs like PiperION® used here is inconclusive (*10, 18, 52-55*). Electron microscopy (Fig. S50A) shows the membrane retains its ~40 μm original thickness in inactive regions remote from the catalyst/ionomer-coated anode, but the sections in contact with the ionomer/catalyst anode thinned and the membrane surface showed fiber-like indentations consistent with the geometry of the PTL (Fig. S51). In AEMWEs without additive, the membrane thickness decreased by 20% and 44% after 20 and 100 h at 2.0 A cm^{-2} and 70 °C, respectively. The loss of membrane thickness was more apparent on the anode-facing side. Membrane thinning/etching was reduced in the AEMWEs with $Zr(OPr)_4$-additive, with 17% and 20% thinning after 20 and 100 h under identical conditions (Fig. S50B).

Gel-permeation chromatography shows the average molecular weight of the ionomer in the membrane from devices with and without $Zr(OPr)_4$ additive decreased after testing for 20 h by 5.7% and 9.9% and after 100 h by 9.7% and 16%, respectively (Fig. S52). As the membrane is not in direct contact with the water-oxidation catalyst, the Zr-additive also appears to slow remote oxidative degradation by decomposing or limiting transport of reactive species. To test this hypothesis, we treated ionomer with and without additive in 1 wt% aq. H_2O_2 at 70 °C for 12 h. NMR analysis showed substantial oxidation of the aromatic region of the ionomer that was largely suppressed for the ionomer sample with Zr-additive (Fig. S9). Similarly, adding 100 ppm H_2O_2 to the anode pure-water feed in the optimal Zr-additive/ionomer device had no apparent effect on durability (Fig. S10).

Chemical interactions between additives and ionomer

Resonant small-angle X-Ray scattering at energies near the Zr K-edge from films of ionomer with $Zr(OPr)_4$-additive (Fig. 4A) shows a prominent peak at q = 0.26 $Å^{-1}$ (d-spacing = 2.4 nm) that is absent in the ionomer-only sample. Nanoscale order appears driven by the interactions with Zr-oxo-oligomers, water, and ionomer and is reminiscent of nanophase separation in perfluorosulfonic acid (Nafion™) ionomers (*56*). This ordering may explain the increased ionic conductivity associated with channels that facilitate OH^- transport. The chemical interactions are evident in infrared spectra (Fig. 4B), which for the as-prepared ionomer have characteristic peaks at 1612 and 1379 cm^{-1} due to asymmetric stretching vibrations of C=O and C–O in HCO_3^- counterions (*57, 58*). With $Zr(OPr)_4$, the intensity of these peaks decreases, while a new peak at 1563 cm^{-1} emerges and intensifies with increasing Zr content, attributed to coordination between Zr^{4+} and CO_3^{2-}. This assignment is supported by spectra of Zr(IV) carbonate basic ($Zr(OH)_2CO_3 \cdot ZrO_2$) with stretches at higher wavenumbers than for Na_2CO_3 (Fig. S56) due to the stronger coordination bonds with higher-valent Zr^{4+} (*59*).

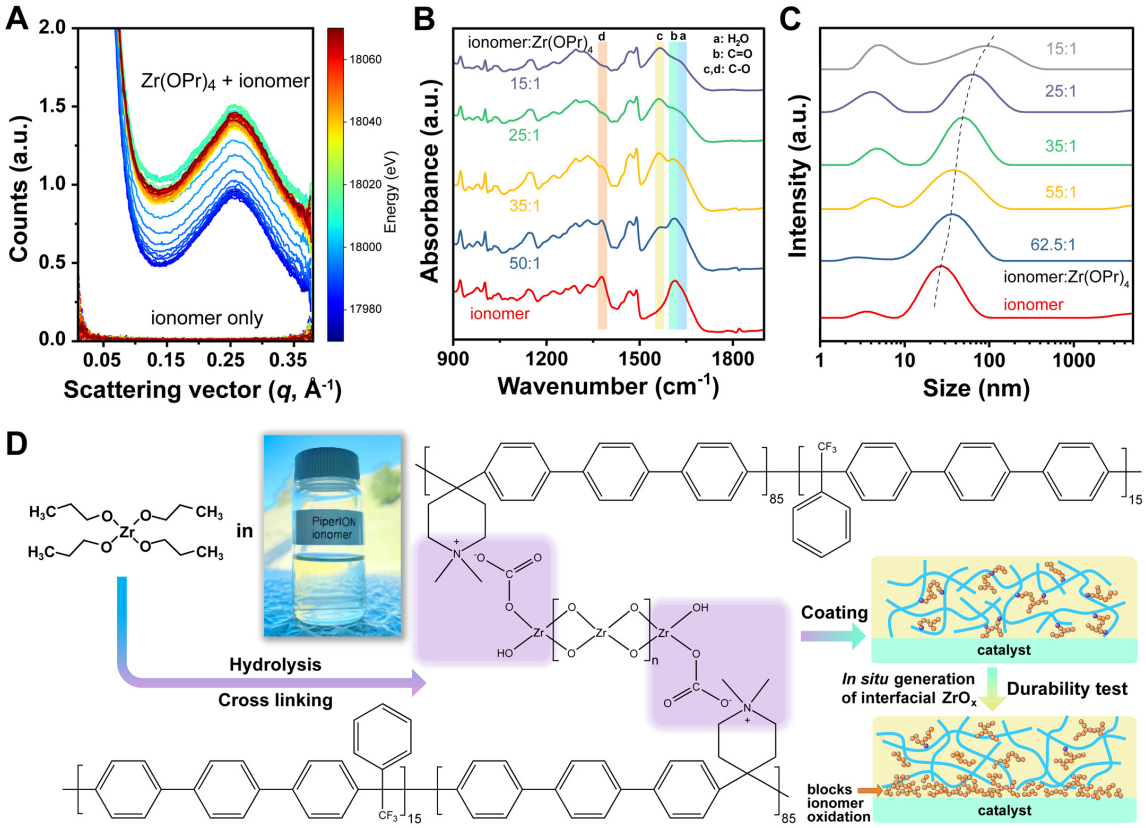

Figure 4. Chemical interactions governing ionomer stabilization by inorganic additive. (**A**) Resonance small-angle X-ray scattering profiles of PiperION ionomer (bottom) and additives/ionomer (top) across the Zr K edge. (**B**) Attenuated total reflectance Fourier-transform infrared spectra of ionomer and additives/ionomer thin films. (**C**) Dynamic-light-scattering analysis of ionomer dispersion and additive/ionomer sol solutions. (**D**) Schematic representation of the additives/ionomer preparation process and the underlying processes leading to protective interphase formation.

The chemical interactions between the additive species derived from $Zr(OPr)_4$ and the ionomer were further evident by dynamic light scattering (DLS). The PiperION® ionomer dispersion in ethanol, diluted with isopropanol to match the concentration in the $Zr(OPr)_4$/ionomer solution, yielded particle-size distributions peaked at 4 nm and 27 nm (Fig. 4C). In the solutions with $Zr(OPr)_4$ added to the ionomer, the primary peak shifts systematically to larger sizes as the ionomer:$Zr(OPr)_4$ ratio decreases, reaching ~100 nm for a ratio of 15:1. These results are consistent with infrared spectra that show the Zr-additive species bind to carbonate counterions with the resulting negatively charged carbonate-capped Zr-oxo oligomers acting as inorganic chemical cross-links between the cationic ionomer backbones. To test this hypothesis, ionomer dispersions with Cl^- counterions were prepared. Minimal chemical interactions between Zr-additive species and ionomer(Cl^-) were found using the same spectroscopy and light-scattering analyses (Fig. S58). With Cl^- counterions (Fig. S59) and $Zr(OPr)_4$, the cell degradation rate was 3.8 ± 1.4 mV h^{-1} over 20 h at 2.0 A cm^{-2}, much higher than when (bi)carbonate was initially present in the ionomer + additive composite. Cryo-TEM analysis (Fig. S60) revealed that the additives/ionomer(Cl^-) yielded Zr-containing nanoparticles resembling those in additives/ionomer(HCO_3^-), but with a less-uniform distribution and aggregation into larger clusters. The precursor structure at the molecular level thus appears important for the formation of stable interphases with the anode

catalyst. As another control, 20-nm ZrO_2 nanoparticles were mixed with ionomer dispersion and coated onto the catalyst surface yielding a similarly high degradation rate of 7.9 mV h^{-1} (Fig. S65). Collectively, these findings highlight the probable role of molecular coordination bonds between the ionomer and Zr-additive species, here through bicarbonate or carbonate, that drive assembly of the inorganic-organic ionically conductive interphase, even though the (bi)carbonate is likely flushed from the system after extended operation.

Conclusion

We introduced and applied interphase engineering to ionomer-based electrochemical devices, yielding more than an order-of-magnitude improvement in durability for AEMWEs operating with pure-water feed. The molecular interactions between inorganic additive species formed via simple and scalable sol-gel chemistry and ionomers are central to creating the robust, ionically conductive material and interphase. During operation, the oxidatively inert ZrO_x inorganic component enriches at the catalyst interfaces and prevents continuous electrochemical oxidative degradation of the ionomer while reinforcing and preserving mechanical stability. Combining these advances with more-active electrocatalysts like high-loading metallic perovskite oxides at the anode (*60*) and optimized PtRu catalysts at the cathode (*61*), alongside passivation layers (*62*) and iterative improvements to ionomer chemistry (*63-65*) may poise pure-water AEMWE as a disruptive commercial electrolysis technology for hydrogen production. More broadly, these approaches could be used to create interphases that control catalyst dissolution/redeposition via confinement (*66*), prevent oxidation side reactions in hydrocarbon-based ionomer devices like PEM fuel cells (*67*), and tune interfacial adhesion and catalyst-layer mechanical properties.

Acknowledgments

We thank G. Freychet for assisting with the collection of X-ray scattering data at Brookhaven National Laboratory. R.T.H. gratefully acknowledges D.H. Marin for insightful discussions regarding the online ICP-MS measurements.

Funding: The electrolyzer device work was supported by the U.S. Department of Energy (DOE), Office of Energy Efficiency and Renewable Energy, award DE-EE0011322. The fundamental work understanding of ionomer-additive and catalyst interface interactions was funded by the DOE Center for Ionomer-Based Water Electrolysis, award DE-AC02-05CH11231. The work made use of the Molecular Foundry, a user facility supported by the DOE under contract DE-AC02-05CH11231. R.T.H., V.C., and T.F.J. acknowledge funding from the Office of Naval Research, grant N00014-24-1-2433, for the design of the online ICP-MS system. Partial support for the online ICP-MS measurements came from the U.S. Department of Energy, Office of Science, Office of Basic Energy Sciences, Chemical Sciences, Geosciences, and Biosciences Division, Catalysis Science Program to the SUNCAT Center for Interface Science and Catalysis. The cryo-TEM and EELS portions of this research were supported by the Center for Nanophase Materials Sciences (CNMS), which is a DOE User Facility at Oak Ridge National Laboratory. Development of X-ray scattering protocols for ionomer composites was supported by the DOE under contract number DE-AC02-05CH11231 within the Inorganic/Organic Nanocomposites Program (KC3104). K.L. and G.M.S. acknowledge support from the Laboratory Directed Research and Development Program of Lawrence Berkeley National Laboratory, DOE contract DE-AC02-05CH11231. This research used the Soft Matter Interfaces beamline at the National Synchrotron Light Source II, a DOE user facility operated under contract DE-SC0012704, and beamline 7.3.3 of the Advanced

Light Source, which is a DOE Office of Science User Facility under contract DE-AC02-05CH11231.

Author contributions: S.H. conceived and designed the experiments and completed most of the synthesis, characterization, and electrolyzer tests. S.W.B. proposed and supervised the entire project. S.H, Y.Z, and S.W.B. wrote the paper with input from all co-authors. A.S. and B.L. performed the SEM cross-section, GPC, and ion exchange capacity for membrane degradation. J.O. and M.J.Z. conducted the cryo-TEM and EELS analyses. M.K. performed cross-sectional electron microscopy and X-ray photoelectron spectroscopy analysis. K.L. and G.M.S. performed X-ray scattering measurements and analysis. P.W. and J.F. contributed to the DLS analysis. R.T.H., V.C., and T.F.J. conducted the online ICP-MS experiments. A.C.E. performed the NMR measurements. H.D. and Y.Y. contributed to the hydroxide conductivity and water uptake experiments. All authors discussed the results and provided editing and comments on the manuscript.

Competing interests: Patent applications were filed on the additive technology (U.S. Provisional Application No. 63/291,295) with some of the co-authors as inventors. A.S. and B.L. are employees of Versogen and Y.Y. is CEO and Founder of Versogen, a company working to commercialize AEMWE technology that makes and markets PiperION membranes and ionomers used in this study. The authors declare that they have no other conflicts of interest.

Data and materials availability: All data are available in the main text or in the supplementary materials. Polarization curves, chronopotentiometry stability data of AEMWE cells, cryo-TEM and SEM images, EDX maps, ATR-FTIR spectra, and DLS data in the main text are openly available in Zenodo (*68*).

References

1. N. Du *et al.*, Anion-Exchange Membrane Water Electrolyzers. *Chem. Rev.* **122**, 11830-11895 (2022).
2. A. Buttler, H. Spliethoff, Current status of water electrolysis for energy storage, grid balancing and sector coupling via power-to-gas and power-to-liquids: A review. *Renew. Sustain. Energy Rev.* **82**, 2440-2454 (2018).
3. D. Li *et al.*, Durability of anion exchange membrane water electrolyzers. *Energy Environ. Sci.* **14**, 3393-3419 (2021).
4. A. Gladik, M. Riedel, R.-A. Eichel, Anion exchange membrane electrolysis at work—Investigating impact of starting parameters and start–stop operation on cold start behavior and degradation. *J. Power Sources* **628**, 235878 (2025).
5. D. Li *et al.*, Highly quaternized polystyrene ionomers for high performance anion exchange membrane water electrolysers. *Nat. Energy* **5**, 378-385 (2020).
6. L. Wang *et al.*, Non-fluorinated pre-irradiation-grafted (peroxidated) LDPE-based anion-exchange membranes with high performance and stability. *Energy Environ. Sci.* **10**, 2154-2167 (2017).
7. Y. Zheng *et al.*, Anion Exchange Ionomers Enable Sustained Pure-Water Electrolysis Using Platinum-Group-Metal-Free Electrocatalysts. *ACS Energy Lett.* **8**, 5018-5024 (2023).

8. M. Klingenhof *et al.*, High-performance anion-exchange membrane water electrolysers using NiX (X = Fe,Co,Mn) catalyst-coated membranes with redox-active Ni–O ligands. *Nat. Catal.* **7**, 1213-1222 (2024).
9. J. R. Varcoe *et al.*, Anion-exchange membranes in electrochemical energy systems. *Energy Environ. Sci.* **7**, 3135-3191 (2014).
10. E. J. Park *et al.*, Aryl ether-free polymer electrolytes for electrochemical and energy devices. *Chem. Soc. Rev.* **53**, 5704-5780 (2024).
11. S. W. Boettcher, Introduction to Green Hydrogen. *Chem. Rev.* **124**, 13095-13098 (2024).
12. P. Mardle, B. Chen, S. Holdcroft, Opportunities of Ionomer Development for Anion-Exchange Membrane Water Electrolysis. *ACS Energy Lett.* **8**, 3330-3342 (2023).
13. R. A. Krivina *et al.*, Anode Catalysts in Anion-Exchange-Membrane Electrolysis without Supporting Electrolyte: Conductivity, Dynamics, and Ionomer Degradation. *Adv. Mater.* **34**, e2203033 (2022).
14. G. Sakas *et al.*, Dynamic energy and mass balance model for an industrial alkaline water electrolyzer plant process. *Int. J. Hydrogen Energy* **47**, 4328-4345 (2022).
15. S. Favero, I. E. L. Stephens, M. M. Titirci, Anion Exchange Ionomers: Design Considerations and Recent Advances - An Electrochemical Perspective. *Adv. Mater.* **36**, e2308238 (2024).
16. N. Chen, Y. M. Lee, Anion exchange polyelectrolytes for membranes and ionomers. *Prog. Polym. Sci.* **113**, 101345 (2021).
17. M. G. Marino, K. D. Kreuer, Alkaline stability of quaternary ammonium cations for alkaline fuel cell membranes and ionic liquids. *ChemSusChem* **8**, 513-523 (2015).
18. Q. Li *et al.*, Ionomer degradation in catalyst layers of anion exchange membrane fuel cells. *Chem. Sci.* **14**, 10429-10434 (2023).
19. J. Wang *et al.*, Poly(aryl piperidinium) membranes and ionomers for hydroxide exchange membrane fuel cells. *Nat. Energy* **4**, 392-398 (2019).
20. W. Song *et al.*, Upscaled production of an ultramicroporous anion-exchange membrane enables long-term operation in electrochemical energy devices. *Nat. Commun.* **14**, 2732 (2023).
21. J. H. Hsu *et al.*, Direct Insertion Polymerization of Ionic Monomers: Rapid Production of Anion Exchange Membranes. *Angew. Chem. Int. Ed.* **62**, e202304778 (2023).
22. W. You, K. J. T. Noonan, G. W. Coates, Alkaline-stable anion exchange membranes: A review of synthetic approaches. *Prog. Polym. Sci.* **100**, 101177 (2020).
23. C. H. Park *et al.*, Nanocrack-regulated self-humidifying membranes. *Nature* **532**, 480-483 (2016).
24. N. Chen *et al.*, Poly(fluorenyl aryl piperidinium) membranes and ionomers for anion exchange membrane fuel cells. *Nat. Commun.* **12**, 2367 (2021).
25. X. Hu *et al.*, An operationally broadened alkaline water electrolyser enabled by highly stable poly(oxindole biphenylene) ion-solvating membranes. *Nat. Energy* **9**, 401-410 (2024).
26. L. Wan *et al.*, Key components and design strategy of the membrane electrode assembly for alkaline water electrolysis. *Energy Environ. Sci.* **16**, 1384-1430 (2023).
27. X. Wu, K. Scott, A Li-doped Co_3O_4 oxygen evolution catalyst for non-precious metal alkaline anion exchange membrane water electrolysers. *Int. J. Hydrogen Energy* **38**, 3123-3129 (2013).

28. L. Xiao *et al.*, First implementation of alkaline polymer electrolyte water electrolysis working only with pure water. *Energy Environ. Sci.* **5**, 7869 (2012).
29. L. Wan *et al.*, Construction of Integrated Electrodes with Transport Highways for Pure-Water-Fed Anion Exchange Membrane Water Electrolysis. *Small* **18**, e2200380 (2022).
30. J. Xiao *et al.*, Water-Fed Hydroxide Exchange Membrane Electrolyzer Enabled by a Fluoride-Incorporated Nickel–Iron Oxyhydroxide Oxygen Evolution Electrode. *ACS Catal.* **11**, 264-270 (2020).
31. A. Li *et al.*, Atomically dispersed hexavalent iridium oxide from MnO_2 reduction for oxygen evolution catalysis. *Science* **384**, 666-670 (2024).
32. R. T. Liu *et al.*, Recent advances in proton exchange membrane water electrolysis. *Chem. Soc. Rev.* **52**, 5652-5683 (2023).
33. G. A. Lindquist *et al.*, Oxidative instability of ionomers in hydroxide-exchange-membrane water electrolyzers. *Energy Environ. Sci.* **16**, 4373-4387 (2023).
34. J. Liu *et al.*, Elucidating the Role of Hydroxide Electrolyte on Anion-Exchange-Membrane Water Electrolyzer Performance. *J. Electrochem. Soc.* **168**, 054522 (2021).
35. N. U. Hassan, Y. Zheng, P. A. Kohl, W. E. Mustain, KOH vs Deionized Water Operation in Anion Exchange Membrane Electrolyzers. *J. Electrochem. Soc.* **169**, 044526 (2022).
36. B. Mayerhöfer *et al.*, Electrochemical- and mechanical stability of catalyst layers in anion exchange membrane water electrolysis. *Int. J. Hydrogen Energy* **47**, 4304-4314 (2022).
37. J. Lim *et al.*, Addressing the Challenge of Electrochemical Ionomer Oxidation in Future Anion Exchange Membrane Water Electrolyzers. *ACS Energy Lett.* **9**, 3074-3083 (2024).
38. D. Li *et al.*, Phenyl Oxidation Impacts the Durability of Alkaline Membrane Water Electrolyzer. *ACS Appl. Mater. Interfaces* **11**, 9696-9701 (2019).
39. E. K. Volk *et al.*, Role of the Ionomer in Supporting Electrolyte-Fed Anion Exchange Membrane Water Electrolyzers. *ACS Electrochem.* **1**, 239-248 (2025).
40. R. A. Krivina *et al.*, Three-Electrode Study of Electrochemical Ionomer Degradation Relevant to Anion-Exchange-Membrane Water Electrolyzers. *ACS Appl. Mater. Interfaces* **14**, 18261-18274 (2022).
41. J. B. Goodenough, K. S. Park, The Li-ion rechargeable battery: a perspective. *J. Am. Chem. Soc.* **135**, 1167-1176 (2013).
42. Y. S. Meng, V. Srinivasan, K. Xu, Designing better electrolytes. *Science* **378**, eabq3750 (2022).
43. X. Fan *et al.*, Fluorinated solid electrolyte interphase enables highly reversible solid-state Li metal battery. *Sci. Adv.* **4**, eaau9245 (2018).
44. Y. Gao *et al.*, Polymer-inorganic solid-electrolyte interphase for stable lithium metal batteries under lean electrolyte conditions. *Nat. Mater.* **18**, 384-389 (2019).
45. B. Jagger, M. Pasta, Solid electrolyte interphases in lithium metal batteries. *Joule* **7**, 2228-2244 (2023).
46. C. J. Brinker, G. W. Scherer, *Sol-gel science: the physics and chemistry of sol-gel processing*. (Academic press, 2013).
47. A. Veyland, L. Dupont, J. Rimbault, J.-C. Pierrard, M. Aplincourt, Aqueous Chemistry of Zirconium(IV) in Carbonate Media. *Helv. Chim. Acta* **83**, 414-427 (2000).
48. K. Li, J. G. Chen, CO_2 Hydrogenation to Methanol over ZrO_2-Containing Catalysts: Insights into ZrO_2 Induced Synergy. *ACS Catal.* **9**, 7840-7861 (2019).
49. L. Chen, Q. Xu, S. W. Boettcher, Kinetics and mechanism of heterogeneous voltage-driven water-dissociation catalysis. *Joule* **7**, 1867-1886 (2023).

50. N. Ziv, D. R. Dekel, A practical method for measuring the true hydroxide conductivity of anion exchange membranes. *Electrochem. Commun.* **88**, 109-113 (2018).
51. M. F. Ernst, V. Meier, M. Kornherr, H. A. Gasteiger, Preparation and Performance Evaluation of Microporous Transport Layers for Proton Exchange Membrane (PEM) Water Electrolyzer Anodes. *J. Electrochem. Soc.* **171**, 074511 (2024).
52. L. Ghassemzadeh, S. Holdcroft, Quantifying the structural changes of perfluorosulfonated acid ionomer upon reaction with hydroxyl radicals. *J. Am. Chem. Soc.* **135**, 8181-8184 (2013).
53. A. Moysiadou, S. Lee, C. S. Hsu, H. M. Chen, X. Hu, Mechanism of Oxygen Evolution Catalyzed by Cobalt Oxyhydroxide: Cobalt Superoxide Species as a Key Intermediate and Dioxygen Release as a Rate-Determining Step. *J. Am. Chem. Soc.* **142**, 11901-11914 (2020).
54. L. Xu, K. H. Moller, J. D. Crounse, H. G. Kjaergaard, P. O. Wennberg, New Insights into the Radical Chemistry and Product Distribution in the OH-Initiated Oxidation of Benzene. *Environ. Sci. Technol.* **54**, 13467-13477 (2020).
55. X. Zhang *et al.*, Effect of Metal Ions on Oxidation of Micropollutants by Ferrate(VI): Enhancing Role of Fe(IV) Species. *Environ. Sci. Technol.* **55**, 623-633 (2021).
56. G. M. Su *et al.*, Chemical and Morphological Origins of Improved Ion Conductivity in Perfluoro Ionene Chain Extended Ionomers. *J. Am. Chem. Soc.* **141**, 13547-13561 (2019).
57. N. J. Firet, W. A. Smith, Probing the Reaction Mechanism of CO_2 Electroreduction over Ag Films via Operando Infrared Spectroscopy. *ACS Catal.* **7**, 606-612 (2016).
58. M. Moradzaman, G. Mul, Infrared Analysis of Interfacial Phenomena during Electrochemical Reduction of CO_2 over Polycrystalline Copper Electrodes. *ACS Catal.* **10**, 8049-8057 (2020).
59. K. D. Dobson, A. J. McQuillan, An Infrared Spectroscopic Study of Carbonate Adsorption to Zirconium Dioxide Sol−Gel Films from Aqueous Solutions. *Langmuir* **13**, 3392-3396 (1997).
60. T. Zhai *et al.*, Perovskite Catalysts for Pure-Water-Fed Anion-Exchange-Membrane Electrolyzer Anodes: Co-design of Electrically Conductive Nanoparticle Cores and Active Surfaces. *J. Am. Chem. Soc.* **147**, 15448-15458 (2025).
61. A. Shirwalkar *et al.*, Comparing Intrinsic Catalytic Activity and Practical Performance of Ni- and Pt-Based Alkaline Anion Exchange Membrane Water Electrolyzer Cathodes. *ACS Energy Lett.* **10**, 1779-1785 (2025).
62. M. Kwak, K. Ojha, M. Shen, S. W. Boettcher, Electrically Insulated Catalyst–Ionomer Anode Interfaces toward Durable Alkaline Membrane Electrolyzers. *ACS Energy Lett.* **9**, 1025-1034 (2024).
63. X. Wu, N. Chen, H. A. Klok, Y. M. Lee, X. Hu, Branched Poly(Aryl Piperidinium) Membranes for Anion-Exchange Membrane Fuel Cells. *Angew. Chem. Int. Ed.* **61**, e202114892 (2022).
64. C. Hu *et al.*, High Free Volume Polyelectrolytes for Anion Exchange Membrane Water Electrolyzers with a Current Density of 13.39 A cm^{-2} and a Durability of 1000 h. *Adv. Sci.* **11**, e2306988 (2024).
65. L. Yin *et al.*, Stable Anion Exchange Membrane Bearing Quinuclidinium for High-performance Water Electrolysis. *Angew. Chem. Int. Ed.* **63**, e202400764 (2024).
66. A. D. Pendergast, S. W. Boettcher, Thrifting iridium for hydrogen. *Science* **387**, 718-719 (2025).

67. Z. Han *et al.*, Hydrocarbon Proton Exchange Membranes for Fuel Cells: Do We Need New Chemical Durability Testing Protocols? *ACS Electrochem.* **1**, 588-598 (2024).
68. S. Hou *et al.*, Dataset of "Durable, pure-water-fed, anion-exchange-membrane electrolyzers through interphase engineering". *Zenodo*, (2025); doi:10.5281/zenodo.14868077.